Effect of strain on the electron effective mobility in biaxially strained silicon inversion layers: An experimental and theoretical analysis via atomic force microscopy measurements and Kubo-Greenwood mobility calculations

Olivier Bonno,[a] Sylvain Barraud, Denis Mariolle, and François Andrieu
CEA/LETI Minatec, 17 rue des Martyrs, 38054 Grenoble, France

(Received 10 October 2007; accepted 15 January 2008; published online 21 March 2008)

Recently, in order to explain the long-channel electron effective mobility at a high sheet carrier density in strained silicon channel transistors, it has been suggested by [M. V. Fischetti, F. Gamiz, and W. Hansch, J. Appl. Phys. **92**, 7230 (2002)] that biaxial tensile strain should smooth the Si/SiO_2 interface. To address this topic, the roughness properties of biaxial strained silicon-on-insulator (s-SOI) films are investigated by means of atomic force microscopy. Through in-depth statistical analysis of the digitalized surface profiles, the roughness parameters are extracted for unstrained and strained SOI films, with 0.8% biaxial tensile strain. Especially, it is found that strain significantly reduces the roughness amplitude. Then, mobility calculations in SOI and s-SOI inversion layers are performed in the framework of the Kubo-Greenwood formalism. The model accounts for the main scattering mechanisms that are dominant in the high electron density range, namely phonon and surface roughness. Special attention has been paid to the modeling of the latter by accounting for all the contributions of the potential which arise from the deformed rough interface, and by using a multisubband wavelength-dependent screening model. This model is then applied to study the influence of the surface morphology on the mobility in s-SOI inversion layers. In this context, the mobility gain between s-SOI and unstrained SOI layers is found to agree significantly better with experimental data if the strain-induced decrease of the roughness amplitude is taken into account.
 [DOI: 10.1063/1.2896589]

I. INTRODUCTION

Aggressive scaling of complementary metal-oxide-semiconductor (CMOS) technology is required so as to meet the International Technology Roadmap of Semiconductors projects in terms of circuit efficiency and device performance.[1] However, to circumvent the downscaling difficulty and extend the lifetime of conventional silicon technology, novel architectures as well as new materials are currently explored. Among the promising avenues, substrates-induced strained silicon (s-Si) layers have generated a great deal of interest owing to both large electron and hole mobility enhancements over unstrained Si layers.[2,3] These s-Si layers are obtained through the pseudomorphic growth of Si epitaxial layers on relaxed SiGe buffers, hence yielding a biaxial tensile strain in the plane normal to the growth direction. There has also been an extensive effort to include strain in the fabrication of silicon-on-insulator (SOI) channel metal-oxide-semiconductor field-effect transistors (MOSFETs), thus benefiting from both the carrier mobility enhancement in s-Si and the advantages of the SOI technology over its silicon counterpart, e.g., a low junction capacitance and better electrostatic control. As a result, many groups have reported both large electron and hole mobility improvements in s-SOI MOSFETs over their conventional SOI architectures. For example, Andrieu *et al.*[4] have demonstrated a 90% electron mobility gain with a TiN/HfO_2 gate stack ($Si_{0.8}Ge_{0.2}$ initial substrate). Among various groups, Rim *et al.* have reported an electron mobility gain up to 125% and a hole mobility enhancement of 21%, using an initial $Si_{0.65}Ge_{0.35}$ substrate.[5]

Modeling tools are highly desirable to serve as guidelines for improving s-SOI channel MOSFETs. However, if the physical picture is clear at a moderate sheet carrier density (i.e., $N_{inv} \sim 10^{12}$ cm^{-2}), the origin of the gain is still not understood at a high electron density ($N_{inv} \geq 10^{13}$ cm^{-2}). Indeed, the electron mobility enhancement in the moderate N_{inv} range is well explained by the strain-induced split of the sixfold degenerate Si conduction-band minima into the well-known Δ_2 and Δ_4 valleys. This band lift leads to a lower conduction-effective mass, as well as a reduction of intervalley scattering, which both increase the mobility in s-SOI channel *n*-MOSFETs.[6] However, the physical mechanisms responsible for the mobility enhancement in s-SOI inversion layers at a large electron density are still unexplained at the moment. At high N_{inv}, in SOI, quantum confinement splits the Δ_2 and Δ_4 valleys, making the strain-induced band lift almost redundant. This should thus strongly reduce the mobility gain in the large N_{inv} region. Yet, many experimental results are in contradiction with this argument since the mobility enhancement is maintained at high N_{inv}.[3–5] The purpose of this work is to investigate this unexplained mobility gain.

It is well known that, at a high carrier density, surface

[a]Author to whom correspondence should be addressed. Telephone: +33 (0) 438 78 20 88. FAX: +33 (0) 438 78 51 40. Electronic mail: olivier.bonno@cea.fr.

roughness (SR) (or, more accurately, interface roughness) is dominant in carrier transport in the channel.[7] Thus, in a recent work, Fischetti *et al.*, after ruling out other possibilities, suggested ascribing the mobility gain to a reduction of the SR scattering with the s-SOI/SiO_2 interface.[8] Expressed otherwise, strain should smooth the s-SOI/SiO_2 interface. Recently, Evans and co-workers have shown, via first-principles modeling, that the SR-limited mobility can be significantly increased thanks to in-plane tensile strain.[9–11]

However, this assumption has not been experimentally verified. To this aim, we report in this work an experimental study of the influence of strain on the surface morphology of s-SOI layers by means of atomic force microscopy (AFM). This technique has been largely used to study Si and s-Si SR.[12–18] Indeed, AFM is particularly useful for analyzing interface roughness because it provides real-space two-dimensional high-resolution topography.[19] In the present work, we investigate the roughness parameters describing the s-SOI surface morphology for 0.8% biaxial tensile strain. Our results show that the roughness amplitude—that describes the fluctuations of the surface heights around the average surface height—is significantly decreased by the strain. Then, we present effective electron mobility calculations using a Kubo-Greenwood model that accounts for the main scattering mechanisms dominant in electron transport at high N_{inv}, i.e., phonons (both acoustic and nonpolar optical) and SR. We investigate the influence on the mobility in s-SOI layers of a modification of the surface morphology. Especially, using the decrease of the roughness amplitude with strain, we show mobility calculations in good agreement with experimental long-channel ones.

The remainder of this article is organized as follows. In Sec. II, the roughness properties of tensively strained SOI substrates are investigated by means of AFM characterization and in-depth statistical analysis. Then, in Sec. III, the Kubo-Greenwood formalism in s-SOI inversion layers is presented. In Sec. IV, mobility calculations in SOI and s-SOI inversion layers are addressed. In this section, the influence of a roughness amplitude modification on the high electron density mobility enhancement factor is discussed. Finally, the main conclusions are summarized in Sec. V.

II. SURFACE MORPHOLOGY OF BIAXIAL TENSILE STRAINED SOI LAYERS

In this section, we present the AFM characterization as well as the statistical analysis of the digitalized AFM topographies. Surface morphology of s-Si films has been investigated both experimentally[12,20] and theoretically[21] in a number of articles. Particularly, it has been shown that strain plays a crucial role in setting the mode of relaxation as well as the surface roughening during the epitaxial growth, depending on the lattice mismatch. Moreover, it has also been shown that the roughness parameters depend on the nature and the deposition process of the gate stack.[22] In this study, we shall quantitatively estimate to which extent the surface morphology of s-SOI compared to that of unstrained SOI is modified by strain. As shown by Goodnick *et al.* in Ref. 23, the roughness measured with AFM does not directly rely on the surface fluctuations really encountered by electrons in the transistor. Yet, the comparison between the roughness of SOI and s-SOI substrates will shed some light on the influence of strain.

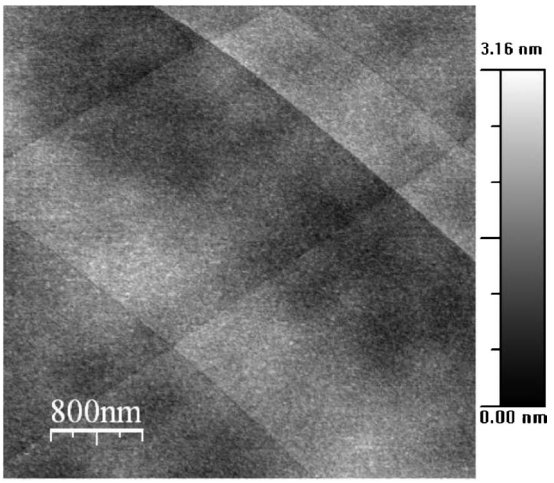

FIG. 1. AFM image of a s-SOI substrate (2×2 μm^2) presenting the so-called cross-hatch pattern that occurs in highly strained silicon growth for a 0.8% biaxial tensile strain. A background removed by a second-order polynomial fit has been performed. Gray scale is given by the surface height.

A. Experimental conditions of AFM imaging

Standard (001) SOI and s-SOI substrates (both with 145 nm buried oxide) have been used for the AFM analysis. For both wafer types, the film thickness is equal to 15 nm. s-SOI substrates have been processed using a relaxed $Si_{0.2}Ge_{0.8}$ virtual substrate as a template. Other details of the fabrication can be found in Ref. 4. AFM measurements were performed with a Digital Instruments Veeco D5000 in the "Tapping^{TM}" mode, with Super Sharp silicon tips used in the standard configuration. An Hf-last surface preparation was carried out on all wafers just before the AFM characterization in order to remove native oxide.

B. AFM results

We report now the results of AFM measurements performed on SOI and s-SOI films. Figure 1 shows a typical AFM image of the s-SOI film for a 2×2 μm^2 scan size with the gray scale in the image determined by the surface height. One can notice in this figure the so-called cross-hatch morphology which commonly occurs in strain layer growth. To avoid the difficulty of isolating a "useful area" between cross-hatch patterns in such a wide scan, we have focused on smaller scan sizes, i.e., in practice, 200 or 500 nm square scanning areas.

Figure 2 shows AFM images of SOI and s-SOI layers (200 nm square scanning area). These surface images are digitized, thus giving an image lattice $h(\mathbf{R})$ on an $N\times N$ two-dimensional mesh, where N is the number of surface sites (in this study, N is 512). Here, $\mathbf{R}=(x,y)$ and $h(\mathbf{R})$ stand for the position wave vector in the plane of the interface and the surface height at position $\mathbf{R}$, respectively. We label the x axis as the AFM tip scanning direction and the y axis as the direction perpendicular to it. For each image, a background subtraction by a second-order polynomial fit has been per-

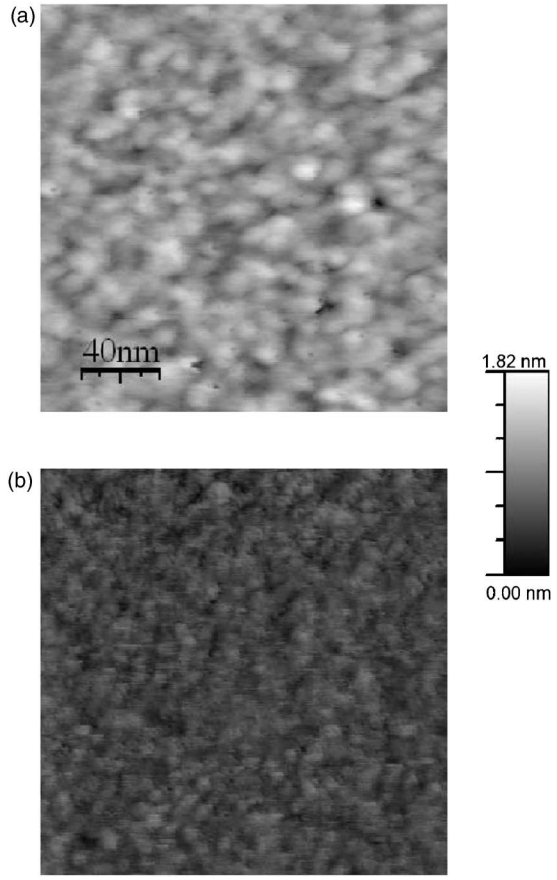

FIG. 2. AFM images (200×200 nm^2) of SOI (a) and s-SOI (b) substrates. The lattice mismatch in the s-SOI film is 0.8%. As in Fig. 1, a background suppression by a least-squares surface fit has been done. The surface height is indicated by the gray scale.

formed to obtain an almost stationary process $h(\mathbf{R})$. This background removal is known to partially suppress long-wavelength fluctuations of the surface.[23] However, as we are mainly interested in short-wavelength roughness, because it corresponds to the studied inversion charge range (high N_{inv} means a short wavelength), this background removal does not alter our conclusions.

To analyze the surface morphology, we first calculate the roughness amplitude, Δ, which is the key parameter to characterize the SR. Δ is defined as the standard deviation of the digitized heights $h(\mathbf{R}_i)$, $i\in\{1,\ldots,N^2\}$, which are treated as a sequence of a random process.[23] Assuming without loss of generality that $h(\mathbf{R})$ has a zero mean, $\Delta^2=\langle h^2(\mathbf{R})\rangle$ where the brackets $\langle\cdots\rangle$ denote ensemble average. To refine the Δ calculation, we follow the method of Yoshinobu *et al.*,[14] averaging the roughness amplitude computed over a series of smaller meshes $(N/2^p)\times(N/2^p)$, with $p=0,1,\ldots,4$. This calculation was also performed over different scan sizes, 200×200 nm^2, 500×500 nm^2, and 2.5×2.5 μm^2. Figure 3 shows the calculated Δ as a function of the length side L of the square scanning area for SOI (closed circles) and s-SOI (open squares). The lattice mismatch in the s-SOI film is $\epsilon=0.8\%$. One can notice that Δ in s-SOI is smaller than Δ in SOI for all scanning areas. For $L=500$ nm, we obtain $\Delta_{\text{s-SOI}}/\Delta_{\text{SOI}}\approx1.7$; this ratio is 1.4 when we average over the three scan areas.

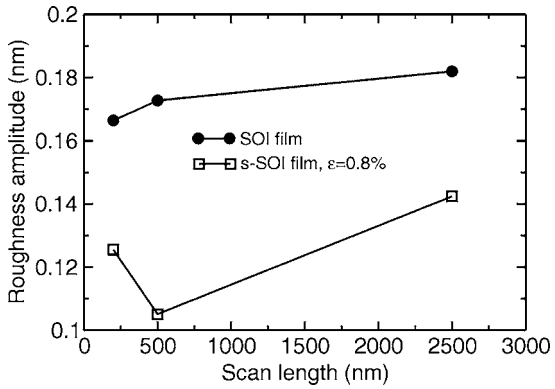

FIG. 3. Roughness amplitude vs the length side of the square scanning area for SOI (closed circles) and s-SOI (open squares) substrates. The lattice mismatch in the s-SOI film is 0.8%.

In order to gain some physical insight concerning the strain dependence of the surface morphology, we study now some important statistical properties of the sequence $h(\mathbf{R})$. To this aim, the so-called height-height correlation function (HHCF), hereafter to be referred to as $\theta(\mathbf{R})$, has been calculated. The HHCF is directly related to the autocorrelation function $C(\mathbf{R})$, since $\theta(\mathbf{R})=2\Delta^2[1-C(\mathbf{R})/\Delta^2]$, and therefore to the power spectrum density (PSD) of the surface via Fourier transform. The PSD is useful since it enters the calculation of the momentum relaxation time relative to SR scattering,[24] and thus is linked to the SR limited mobility, μ_{SR}. Therefore, a modification of the HHCF results in a mobility change, especially at large N_{inv}. The HHCF is defined as[19]

$$\theta(\mathbf{R})=\langle[h(\mathbf{R}')-h(\mathbf{R}+\mathbf{R}')]^2\rangle, \tag{1}$$

where it is always assumed that $h(\mathbf{R})$ is a zero mean process. Due to the degraded correlation in the direction perpendicular to the scan axis, we performed an average over the y direction. Hence, instead of $\theta(\mathbf{R})$, we consider $\tilde{\theta}(x)$ defined as

$$\tilde{\theta}(x)=\langle\langle[h(x',y)-h(x+x',y)]^2\rangle_{x'}\rangle_y. \tag{2}$$

In Fig. 4, we plot $\tilde{\theta}$ as a function of the distance along the tip-scanning direction for SOI and s-SOI ($\epsilon=0.8\%$) layers computed via the 200×200 nm^2 scan size. As in the limit $x\to\infty$, $\tilde{\theta}(x)$ obeys the property: $\tilde{\theta}(x\to\infty)\to2\Delta^2$, one can readily verify in Fig. 4 that Δ decreases with the strain. Moreover, with $\tilde{\theta}(x)$ it is possible to calculate the so-called correlation length Λ.[19] This quantity is a measure of the range over which the surface heights are not completely independent.[23,24] In the literature,[23] the HHCF has been successfully described in terms of a simple exponential function written as

$$\tilde{\theta}(x)=2\Delta^2\left\{1-\exp\left[-\left(\frac{x}{\Lambda}\right)\right]\right\}. \tag{3}$$

Using Eq. (3), $\Lambda=4.1$ nm and $\Lambda=2.8$ nm were calculated for the SOI and s-SOI films, respectively. These results demonstrate that strain modifies not only Δ but also Λ. However, it should be noted that an accurate determination of the cor-

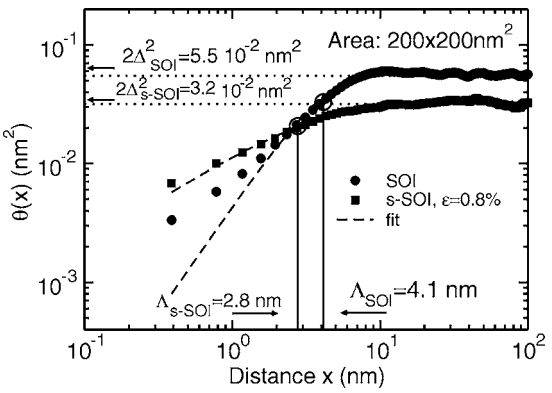

FIG. 4. Averaged height-height correlation function $\tilde{\theta}(x)$ [see Eq. (2) for definition] as a function of the distance along the tip scanning direction for the SOI (closed circles) and s-SOI (closed squares) 200×200 nm^2 scan. The lattice mismatch in the s-SOI film is 0.8%. The extracted values of the correlation length Λ calculated using Eq. (3) as a fit (dashed lines) are also indicated.

relation length is much more difficult to obtain than that of the roughness amplitude. Indeed, Goodnick *et al.*[23] have shown that Λ is strongly altered by the statistical analysis; the order of the background polynomial fit, the available window length of the random process, or the HHCF modeling are some examples of parameters that significantly modify the determination of Λ. Consequently, the uncertainty in the determination of Λ makes the comparison between SOI and s-SOI quite delicate. In this regard, another argument can be put forward through reasoning about μ_{SR}. Among other quantities, μ_{SR} is mainly determined by the PSD, $S(Q)$, since $\mu_{SR}\propto\tau_{SR}\propto 1/S$. The two-dimensional PSD corresponding to the HHCF expression Eq. (3) is given by[19]

$$S(Q)=\frac{2\pi\Delta^2\Lambda^2}{(1+Q^2\Lambda^2)^{3/2}}. \tag{4}$$

Thanks to this formula, one understands that the two roughness parameters, Δ and Λ, influence μ_{SR} differently. While μ_{SR} is proportional to Δ^{-2} irrespective of the N_{inv} value, the relationship between μ_{SR} and Λ depends strongly on N_{inv}. Indeed, as already pointed out by Fischetti *et al.*,[8] when screening effects are neglected, the Λ-dependence of μ_{SR} is changed at the key density $N_{SR}\approx 1/(\pi\Lambda)^2$ from $\mu_{SR}\propto\Lambda^{-2}$ to $\mu_{SR}\propto\Lambda$. However, when no assumption is made about dielectric screening, the Λ-dependence of μ_{SR} is not so obvious. Moreover, experimental results have shown that, contrary to μ_{SR}, the mobility enhancement in s-SOI inversion layers does not depend on the electron density. For all these reasons, we will concentrate on the Δ-dependence of μ_{SR}, which is certainly much easier to catch, keeping in mind that other parameters such as Λ may play a significant role too. Efforts to understand the influence of Λ are planned in future works.

Our AFM measurements show that in-plane tensile strain in silicon significantly affects the surface morphology. Particularly, the roughness amplitude Δ is decreased when strain increases. However, this parameter strongly influences the mobility. The purpose of the next sections is to quantify the evolution of the s-SOI mobility with Δ in the high electron density limit.

III. EFFECTIVE ELECTRON MOBILITY

To distinguish among the possible mechanisms that could explain the high field electron mobility enhancement ratio, the temperature dependence of the electron effective mobility in (s-)SOI inversion layers has been computed and compared to experimental measurements.[18] In this section, we describe the model used to calculate the electron effective mobility in (s-)SOI inversion layers.

A. The Kubo-Greenwood model

The effective mobility in the (s-)SOI inversion layer is calculated using the Kubo-Greenwood formulation within the framework of a two-dimensional electron gas. This formalism has been extensively outlined in a number of articles;[6,25–27] however, let us recall the basic steps of the calculation. The preliminary stage of the mobility computation is the determination of the eigenstates and eigenvalues of the (s-)SOI inversion layer by solving the Schrödinger equation. In order to account for space-charge effects, this determination is coupled with the Poisson equation in a self-consistent manner.[28] The energies and wave functions obtained are then used to calculate the momentum relaxation times, which are the basic ingredients of the Kubo-Greenwood model. In this study, we have considered intravalley scattering with acoustic phonons, intervalley scattering with nonpolar optical phonons, and SR scattering. As we mainly focus on the large N_{inv} mobility regime, impurity scattering has been disregarded in this work since it is known to limit the mobility only at low N_{inv}.[6,7]

Let us briefly outline the mobility formulation in the Kubo-Greenwood formalism. We consider the (s-)SOI/SiO_2 interface to be parallel to the (001) crystal plane, so the z axis—the confinement direction—is along the [001] direction. We label the x axis as the source-to-drain direction and the y axis as the direction perpendicular to it, namely the [100] and [010] directions, respectively.[29] Among the components of the mobility tensor,[26] we shall calculate only the component μ_{xx} of the mobility tensor, i.e., the diagonal component along the longitudinal field. For simplicity, we just refer to this term as μ. The mobility is thus expressed as[27]

$$\mu=\sum_{\xi}\frac{e_0 g_\xi}{2\pi^2\hbar^2 N_{inv}k_B T}\times\int_0^{2\pi}d\beta\int_0^{\infty}\Omega_{\xi,x,y}(\varepsilon,\beta)\tau_{x,\xi}(\varepsilon,\beta)f_\xi(\varepsilon)[1-f_\xi(\varepsilon)]d\varepsilon, \tag{5}$$

where ε and β are the kinetic energy and the polar angle, respectively, e_0 is the elementary electronic charge, $\hbar$ is the reduced Planck constant, k_B is the Boltzmann constant, T is the lattice temperature, g_ξ is the degeneracy of the ξth subband including spin, $\tau_{x,\xi}(\varepsilon,\beta)$ is the relaxation time for the xth component of the momentum in subband ξ, $f_\xi(\varepsilon)$ is the Fermi-Dirac distribution,

TABLE I. Set of physical parameters used in the present calculations.

Quantity	Symbol	Value	Unit	Reference
Static permittivity	ε_r	11.7	8.854×10^{-12} F/m	25
Density	ρ	2.3×10^3	kg m^{-3}	38
Longitudinal sound velocity	v_l	9×10^3	m s^{-1}	25
Transverse sound velocity	v_t	5.4×10^3	m s^{-1}	25
Uniaxial-shear deformation potential	Ξ_u	9.8	eV	39
Elastic constants				
	c_{11}	16.577	10^{11} dyn/cm^2	38
	c_{12}	6.393	10^{11} dyn/cm^2	38
Acoustic deformation potential	D_{ac}	10	eV	8
Nonparabolicity coefficient	γ	0.5	eV^{-1}	25
Optical phonon deformation potentials	⋯	⋯	⋯	43

$$f_\xi(\varepsilon)=\frac{1}{1+\exp\left(\dfrac{\varepsilon+e_\xi-E_F}{k_BT}\right)}, \tag{6}$$

and $\Omega_{\xi,x,y}(\varepsilon,\beta)$ is detailed below. In Eq. (6), E_F is the Fermi level and e_ξ is the eigenvalue of the ξth subband. The term $\Omega_{\xi,x,y}(\varepsilon,\beta)$ results from the anisotropy of the effective mass tensor. Using a nonspherical, nonparabolic dispersion relation in the above-chosen coordinate system, it is expressed as

$$\Omega_{\xi,x,y}(\varepsilon,\beta)=\varepsilon(1+\gamma\varepsilon)(1-2\gamma\varepsilon)\frac{\cos^2\beta}{m_{\xi,x}^2}\times\left(\frac{\cos^2\beta}{m_{\xi,x}}+\frac{\sin^2\beta}{m_{\xi,y}}\right)^{-2}, \tag{7}$$

where $m_{\xi,x}$ and $m_{\xi,y}$ are the electron effective masses of subband ξ along the x and y axes, respectively, and γ is the nonparabolicity coefficient. To obtain Eq. (7), it was assumed that the dispersion relation in subband ξ is written as

$$\frac{\hbar^2K^2}{2}\left(\frac{\cos^2\beta}{m_{\xi,x}}+\frac{\sin^2\beta}{m_{\xi,y}}\right)=\varepsilon_\xi(\mathbf{K})[1+\gamma\varepsilon_\xi(\mathbf{K})],$$

where (K,β) are the polar coordinates of the two-dimensional wave vector $\mathbf{K}$.

B. Relaxation rates

The momentum relaxation rates relative to phonons (considering both acoustic and optical modes) are treated following the approach described in Refs. 26 and 30, with the parameters listed in Table I. Regarding the acoustic phonon model, keeping in mind that we aim to compare the mobility calculations with the experimental data for various lattice temperatures, the dispersion of the acoustic phonon energy has been taken into account, beyond the so-called equipartition approximation.[31,32] Hence, the acoustic phonon dispersion is approximated by $\hbar\omega_{ac}(\mathbf{q})\approx\hbar v_s q$, where v_s is the sound velocity and $\mathbf{q}$ the three-dimensional exchanged phonon wave vector.

The momentum relaxation rate due to interface-roughness scattering is calculated using the formulation of Ando *et al.*,[24] later used by many authors.[27,33–35] However, from the linearization of the two-dimensional Boltzmann transport equation, the SR relaxation time can only be defined implicitly via a system of integral equations that relates the relaxation times of the different subbands (see Ref. 27, for example). In order to simplify the problem, the implicit expression of the SR relaxation time has been assumed in this study. This simplification, embraced by many authors in the past, does not introduce significant errors in the determination of μ. Thus, the SR momentum relaxation rate for an electron of wave vector $\mathbf{K}$ in subband ξ is given by

$$\frac{1}{\tau_{x,\xi}^{SR}(\mathbf{K})}=\frac{1}{2\pi\hbar^3}\sum_{\xi'}\Theta[E_\xi(\mathbf{K})-e_{\xi'}]\{1+2\gamma[E_\xi(\mathbf{K})-e_{\xi'}]\}\times\int_0^{2\pi}d\beta'\left(\frac{\cos^2\beta'}{m_{\xi',x}}+\frac{\sin^2\beta'}{m_{\xi',y}}\right)^{-1}\times|\Gamma_{\xi\xi'}^{scr}(Q)|^2S(Q)\left[1-\frac{K'}{K}\cos(\beta-\beta')\right], \tag{8}$$

where $\mathbf{K}'$ is the final wave vector, $\Theta(w)$ is the Heaviside step function, $E_\xi(\mathbf{K})=e_\xi+\varepsilon_\xi(\mathbf{K})$ is the total energy, $\mathbf{Q}=\mathbf{K}-\mathbf{K}'$ is the exchanged wave vector, $\Gamma_{\xi\xi'}^{scr}(Q)$ is the screened SR potential matrix element, $S(Q)$ is the PSD, and finally, β' is the polar angle of $\mathbf{K}'$. We recall that the two-dimensional PSD is given by

$$S(Q)=\frac{2\pi\Delta^2\Lambda^2}{(1+Q^2\Lambda^2)^{3/2}}.$$

To conclude the description of the model, let us briefly specify a few remarks about the modeling of the SR scattering. The SR scattering potential used to compute the unscreened matrix elements $\Gamma_{\xi\xi'}^{unscr}(Q)$ involves three contributions (see Ref. 27 for further details): (i) a first term representing the direct scattering with the interfacial "steps;" (ii) a second term due to the shift of the electron density along the confinement direction; and finally (iii) the potential arising from the dipole moments induced by the deformed rough interface.[24] In the present study, the expressions of the "kind (ii) and (iii) terms" detailed by Fischetti *et al.*,[27] as well as the refined formulation of the kind (i) contribution recently proposed by Esseni in Ref. 36, are used. In order to calculate the SR screened potential matrix elements, the inversion of the multisubband dielectric matrix is numerically performed. The Maldague's static wavelength-dependent expression is used to compute the diagonal elements of the

polarizability,[37] improved to account for nonparabolicity. To this aim, instead of the nonparabolic density of states employed in Ref. 37, $\partial n_\xi / \partial E_F$ is used, where n_ξ is the electron sheet density of the ξth subband, namely

$$n_\xi = g_\xi \frac{(m_{\xi,x} m_{\xi,y})^{1/2}}{2\pi\hbar^2} k_B T [\mathcal{F}_0(\eta_\xi) + 2\gamma k_B T \mathcal{F}_1(\eta_\xi)],$$

where $\eta_\xi = (E_F - e_\xi)/(k_B T)$ and $\mathcal{F}_\beta$ is the Fermi integral of order β. Moreover, following Fischetti and colleagues, nondiagonal terms of the polarizability matrix have been neglected.[8] Finally, it is assumed that simultaneously present scattering rates can be added, i.e., the well-known Matthiessen's rule is applied in each subband.[8]

C. SOI and s-SOI material parameters

In the simulation, the (001) in-plane strain-induced lift, $\Delta E_{2/4}^{\mathrm{str}}$, between the Δ_4 and Δ_2 valleys is accounted for using the following expression:

$$\Delta E_{2/4}^{\mathrm{str}}(\epsilon) = \Xi_u \left(\frac{2c_{12}}{c_{11}} + 1 \right) \epsilon, \tag{9}$$

where c_{ij} are the elastic constants of Si and Ξ_u is the silicon uniaxial-shear deformation potential.[38] The strain also modifies the Si band curvature, e.g., the effective masses. These changes, although quite slight for (001) tensile in-plane strain in Si, have been taken into account following the data of Ref. 39. The parameters used in the mobility computation (except roughness ones; see the discussion below) are rather standard and listed in Table I.

IV. RESULTS

In this section, we report mobility calculations in (s-)SOI inversion layers using the model described previously. After the calibration of the model, the influence of the roughness amplitude on the mobility gain at a high electron sheet density is then studied.

A. Simulated device structure

The device simulated in this study consists of a (s-)SOI film of thickness $W=15$ nm sandwiched between a 145 nm thick buried oxide and a 1 nm thin oxide layer (both being in SiO_2). The material gate is polysilicon. As in Ref. 8, a uniform doping concentration of $N_A = 3 \times 10^{17}$ cm^{-3} has been assumed. Three subbands in each valley have been considered to keep the computational cost reasonable. However, it has been verified using more subbands that calculations performed with three subbands are still accurate. Unless otherwise specified, all calculations are carried out using the Goodnick's PSD model [i.e., Eq. (4)].

To begin with, we present the calculated potential of Δ_2 valley, $V(z)$, and wave functions, $\Psi_\xi(z)$, for the simulated structure considering the unstrained and strained cases. Therefore, Fig. 5 shows the Δ_2 conduction band profile and the first two wave functions of both the Δ_2 and Δ_4 valleys considering $\epsilon=0$ [Fig. 5(a)] and $\epsilon=0.8\%$ [Fig. 5(b)] s-SOI film. The sheet density is 10^{13} cm^{-2} and the temperature 300 K. It is seen in Fig. 5(a) that for $\epsilon=0$ the Fermi level E_F is

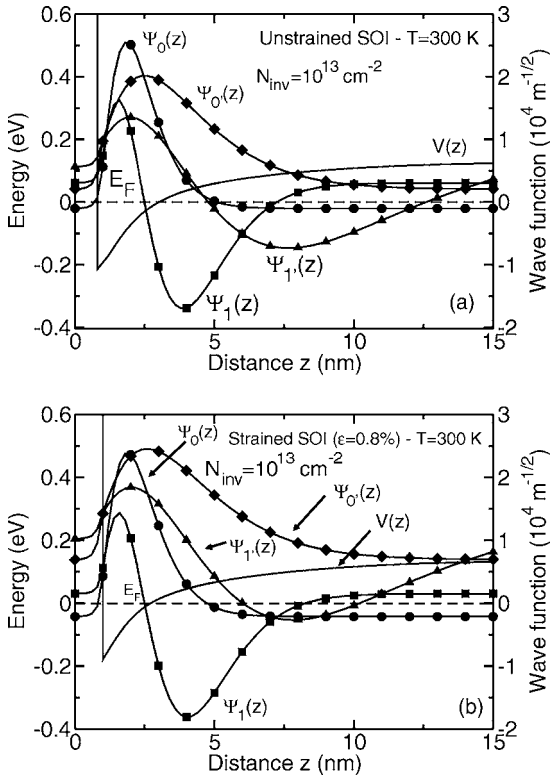

FIG. 5. Conduction band profile of Δ_2 valley [denoted as $V(z)$, solid line] and wave functions [labeled by $\Psi_\xi(z)$, closed symbols] for the Δ_2 (unprimed index) and Δ_4 (primed index) valleys in an unstrained (a) and strained (b) SOI film of thickness $W=15$ nm. The potential and wave functions are obtained through a self-consistent resolution of Schrödinger and Poisson equations. The electron sheet density is 10^{13} cm^{-2} and the temperature 300 K. The wave functions have been shifted so that their respective zeros correspond to the quantized energy levels. The energy reference in each graph is the Fermi level E_F (dashed line). The lattice mismatch in the s-SOI layer is 0.8%. Finally, note that energies (respectively, wave functions) are referenced to the left (respectively, right) axis.

very close to the fundamental levels of the Δ_2 and Δ_4 valleys (i.e., e_0 and $e_{0'}$), so that the major part of the carriers is in these two subbands. However, at $\epsilon=0.8\%$, E_F is situated near the subbands e_0 and e_1 that both receive most of the sheet density. To summarize, in unstrained SOI the mobility will have a Δ_2 as well as a Δ_4 contribution, while in s-SOI the mobility will result almost solely from a Δ_2 contribution.

B. The SOI mobility

We followed the same approach as Fischetti and co-workers.[8] Thus, we first adjusted Δ and Λ so as to reproduce the experimental SOI mobility at high N_{inv} (Ref. 40) at 300 K. To this aim, we plot in Fig. 6 the electron mobility in an unstrained SOI inversion layer versus the electron density at 300 K. One can observe a good agreement between the theoretical mobility (solid line) and the experimental data (closed circles) for $\Delta_{\mathrm{SOI}}=0.3$ nm and $\Lambda_{\mathrm{SOI}}=1.3$ nm. These values are within the range of the scattered values found in the literature (see, e.g., Refs. 8 and 30).

However, one may object that the estimated roughness parameters obtained via mobility fit do not precisely agree with those previously extracted through AFM measurements, i.e., $\Delta \approx 2$ Å and $\Lambda \approx 4.1$ nm. This fact has been extensively

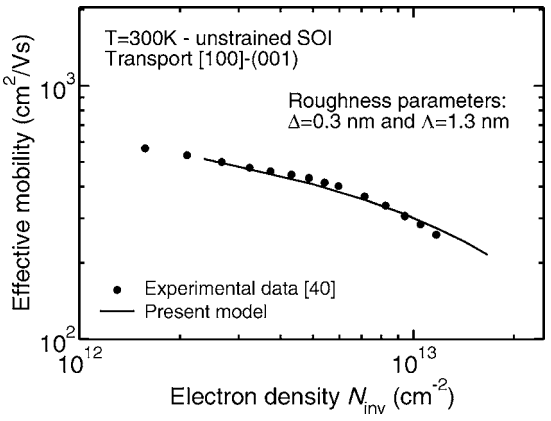

FIG. 6. Calculated effective mobility (solid line) as a function of the electron density in an unstrained SOI inversion layer of thickness $W=15$ nm at 300 K. The experimental data (closed circles) are those of Esseni *et al.* (Ref. 40).

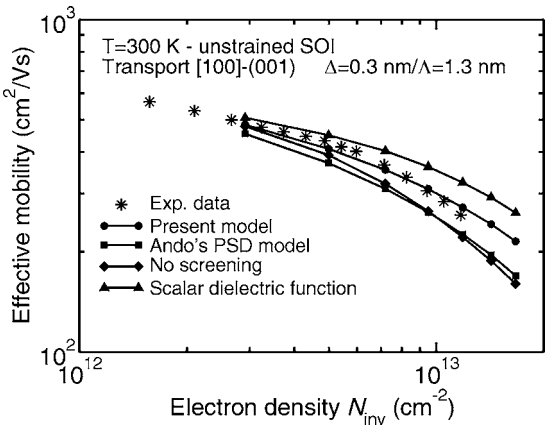

FIG. 7. Effective mobility as a function of the electron density in an unstrained SOI inversion layer for different SR scattering models. Circles: the complete model of Fig. 6; Squares: Ando's PSD model; Diamonds: without screening; Upper triangles: dielectric screening by the fundamental subband of Δ_2 valley using a wavelength-independent polarizability. The stars denote the experimental data of Ref. 40. The closed symbols are calculated values; the lines are only a guide to the eye.

discussed by Goodnick and colleagues,[23] who enumerate the reasons that could explain this unsatisfactory agreement. On the one hand, the roughness parameters strongly depend on the other parameters used in the calculation, such as the acoustic and optical deformation potentials, sound velocities, effective masses. So far, the choice of the set of material parameters is still the subject of some debate, concerning in particular phonon coupling constants, e.g., depending on the authors, acoustic deformation potentials ranging from 6.6 eV up to 14.6 eV have been reported.[6,30,38] On the other hand, there are also statistical reasons explaining this discrepancy. They result from the limited number of sampled heights $h(\mathbf{R}_i)$ that are available to accurately determine Δ and Λ (see Ref. 23 for a complete review of this topic). Moreover, it should be noted that Δ and Λ have been extracted using surface measurements that do not take into account all the steps of the elaboration process of the device, especially the influence of the gate stack via the so-called remote roughness scattering.[34] Hence, the modeling of the interface-roughness scattering is certainly simplified, making the agreement between the mobility fit and AFM extracted roughness parameters somewhat difficult and questionable. However, in the present study, we discuss the strain-induced modification by comparing SOI and s-SOI devices fabricated using the same conditions. Therefore, both SOI/SiO_2 and $s\text{-}SOI/SiO_2$ interfaces are identically simplified. This justifies our approach based on a comparison between the roughness parameters in SOI and s-SOI.

C. Discussion about the SR-limited mobility

To investigate the influence of the SR scattering model on the roughness parameters, Fig. 7 presents the effective mobility obtained with the same parameters Δ and Λ as in Fig. 6 but using different models of the SR scattering. We consider the three following variants of the complete model (circles): (i) Ando's PSD model (squares); (ii) no screening (diamonds); (iii) screening by one subband, chosen to be the first subband of the Δ_2 valley, with a wavelength-independent polarizability (upper triangles). While the same set of roughness parameters is used, one can observe that the mobility can be significantly altered by the modeling of the SR-limited mobility. A modification in the screening or the polarizability model leads to an under- or overestimation of the mobility by about 20% at $N_{inv}=10^{13}$ cm^{-2}. As a consequence, the determination of Δ that best agrees with the experimental data (stars in Fig. 7) can be modified by at least 5% depending on the scattering model (i)–(iii).

D. Temperature dependence of the mobility gain

Let us now focus on the physical mechanisms responsible for the mobility enhancement factor at high N_{inv}. Figure 8 shows the mobility gain, namely the ratio between the mobility in s-SOI over the one in SOI as a function of the temperature for $N_{inv}=10^{13}$ cm^{-2}. The calculations have been performed accounting for strain only through the $\Delta_2-\Delta_4$ band split and through the minor changes of the s-Si band structure (see Sec. III C). At 300 K, it is readily seen that the calculated gain is much smaller (almost a factor of 2) than the experimental one, an observation still made by Fischetti and co-workers.[27] The disagreement between the theoretical and the experimental mobility gain is maintained over the

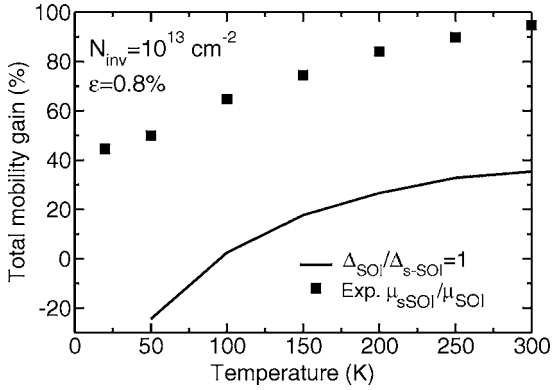

FIG. 8. Total mobility gain as a function of the lattice temperature. The closed symbols are the experimental measurements (Ref. 18). The electron density is $N_{inv}=10^{13}$ cm^{-2}. The lattice mismatch in the s-SOI layer is 0.8%.

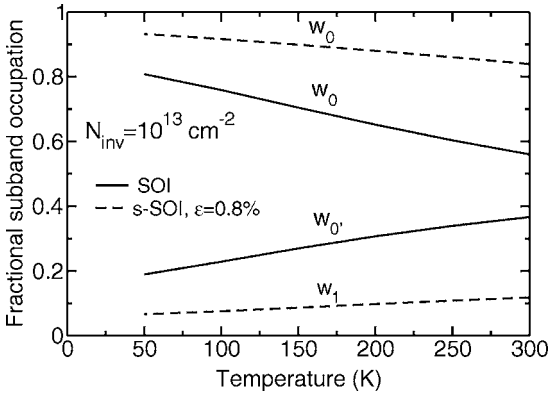

FIG. 9. Fractional subband populations w_ξ as a function of the temperature for an unstrained (solid line) and strained (dashed line) SOI inversion layer. Unprimed (primed) index stands for subbands of the $\Delta_2(\Delta_4)$ valley. The lattice mismatch in the s-SOI layer is 0.8%.

whole temperature range. However, the decrease of the mobility enhancement ratio with the temperature presents the correct behavior exhibited by the experimental data. This is mainly due to a subband population modulation which can be observed in Fig. 9. This figure displays the fractional subband occupation as a function of the temperature for the SOI and s-SOI inversion layer at $N_{\text{inv}}=10^{13}$ cm^{-2}. This strain-induced "repopulation" yields a lower conduction effective mass and a decrease of SR scattering via screening effects that together explain the reduction of the mobility enhancement factor with the temperature.

As suggested by Fischetti *et al.*[27] and confirmed by our AFM measurements, the mobility gain has to be computed using a reduced roughness amplitude for the mobility calculation in the s-SOI inversion layer. Thus, Fig. 10 shows the mobility gain versus the temperature, using two values of $a=\Delta_{\text{SOI}}/\Delta_{\text{s-SOI}}$, namely $a=1$ (same as Fig. 8, solid line) and $a=1.4$ (AFM results, dashed line). A better agreement with the experimental data is noticed when the strain-induced decrease of the roughness amplitude is accounted for. This confirms that the mobility gain at a high electron density is due to the smoothness of the s-SOI/SiO_2 interface.

V. CONCLUSION

In this work, AFM measurements of unstrained and 0.8% biaxially tensile strained SOI films have been carried out. Through in-depth statistical analysis, it has been demonstrated that strain reduces the roughness amplitude by about 30%.

Then, mobility calculations in SOI and s-SOI inversion layers have been performed using the Kubo-Greenwood formalism. The model includes the main scattering mechanisms, especially SR, using a detailed model that takes into account all contributions of the perturbing potential induced by the deformed rough interface. It is shown that modeling strain only through the band splitting of the sixfold degenerate silicon conduction band minima is not sufficient to reproduce the high mobility enhancement ratio of ~90% at 300 K and ~40% at 20 K, in the high electron sheet density regime, around 10^{13} cm^{-2}. However, using the inputs of the AFM characterization, it is shown that the mobility gain in the high inversion charge range is due to a strain-induced decrease of the roughness amplitude.

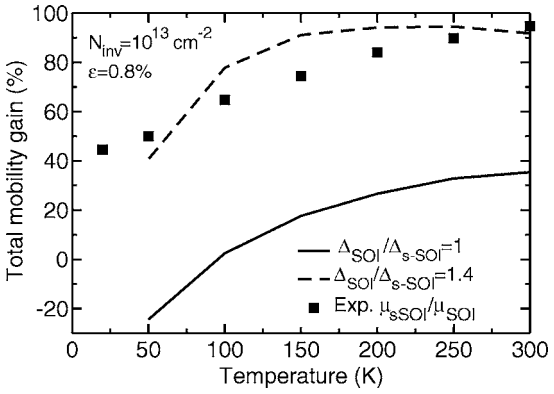

FIG. 10. Total mobility gain as a function of the lattice temperature. Same as Fig. 8 but using different values of $a=\Delta_{\text{SOI}}/\Delta_{\text{s-SOI}}$. The closed squares are the experimental measurements (Ref. 18). Solid line: $a=1$; dashed line: $a=1.4$.

ACKNOWLEDGMENTS

This work was partially supported by the French R3N under the project *Modern* and the European Medea+ under the project *Silonis*. The authors gratefully acknowledge use of the LETI facilities for device processing.

[1]See, e.g., International Roadmap for Semiconductors 2005, http://www.itrs.net/Links/2005ITRS/Home2005.htm
[2]I. Lauer, T. Langdo, Z.-Y. Cheng, J. Fiorenza, G. Braithwaite, M. Currie, C. Leitz, A. Lochtefeld, H. Badawi, M. Bulsara, M. Somerville, and D. Antoniadis, IEEE Electron Device Lett. **25**, 83 (2004).
[3]M. L. Lee, E. A. Fitzgerald, M. T. Bulsara, M. T. Currie, and A. Lochtefeld, J. Appl. Phys. **97**, 011101 (2005).
[4]F. Andrieu, C. Dupre, F. Rochette, O. Faynot, L. Tosti, C. Buj, E. Rouchouze, M. Cassé, B. Ghyselen, I. Cayrefourcq, L. Brévard, F. Allain, J.-C. Barbé, J. Cluzel, A. Vandooren, S. Denorme, T. Ernst, C. Fenouillet-Béranger, C. Jahan, D. Lafond, H. Dansas, B. Previtali, J. P. Colonna, H. Dampreix, P. Gaud, C. Mazuré, and S. Deleonibus, in 2006 Symposium on VLSI Technology Digest (IEEE, Piscataway, NJ, 2006), p. 168.
[5]K. Rim, K. Chan, L. Shi, D. Boyd, J. Ott, N. Klymko, F. Cardone, L. Tai, S. Koester, M. Cobb, D. Canaperi, B. To, E. Duch, I. Babich, R. Carruthers, P. Saunders, G. Walker, Y. Zhang, M. Steen, and M. Ieong, in Technical Digest–International Electron Device Meeting (2003), p. 49.
[6]S.-I. Takagi, J. L. Hoyt, J. J. Welser, and J. F. Gibbons, J. Appl. Phys. **80**, 1567 (1996).
[7]S.-I. Takagi, A. Toriumi, M. Iwase, and H. Tango, IEEE Trans. Electron Devices **41**, 2357 (1994).
[8]M. V. Fischetti, F. Gamiz, and W. Hansch, J. Appl. Phys. **92**, 7320 (2002).
[9]M. H. Evans, X.-G. Zhang, J. D. Joannopoulos, and S. T. Pantelides, Phys. Rev. Lett. **95**, 106802 (2005).
[10]M. H. Evans, M. Caussanel, R. D. Schrimpf, and S. T. Pantelides, in Technical Digest–International Electron Devices Meeting (2005), p. 597.
[11]S. T. Pantelides, G. Hadjisavvas, M. H. Evans, L. Tsetseris, M. Caussanel, and R. D. Schrimpf, ECS Trans. **6**, 353 (2007).
[12]R. M. Feenstra, M. A. Lutz, F. Stern, K. Ismail, P. M. Mooney, F. K. LeGoues, C. Stanis, J. O. Chu, and B. S. Meyerson, J. Vac. Sci. Technol. B **13**, 1608 (1995).
[13]N. Sugii, K. Nakagawa, S. Yamaguchi, and M. Miyao, Appl. Phys. Lett. **75**, 2948 (1999).
[14]T. Yoshinobu, A. Iwamoto, K. Sudoh, and H. Iwasaki, J. Vac. Sci. Technol. B **13**, 1630 (1995).
[15]T.-S. Yoon, J. Liu, A. M. Noori, M. S. Goorsky, and Y.-H. Xie, Appl. Phys. Lett. **87**, 012014 (2005).
[16]E. Escobedo-Cousin, S. H. Olsen, S. J. Bull, A. G. O'Neill, H. Coulson, C. Claeys, R. Loo, R. Delhougne, and M. Caymax, in SiGe Technology and Device Meeting 2006 (2006), Vol. 1.
[17]A. Pirovano, A. L. Lacaita, G. Ghidini, and G. Tallarida, IEEE Electron Device Lett. **21**, 34 (2000).
[18]O. Bonno, S. Barraud, F. Andrieu, D. Mariolle, F. Rochette, M. Cassé, J. M. Hartmann, F. Bertin, and O. Faynot, in 2007 Symposium on VLSI

Technology Digest (IEEE, Piscataway, NJ, 2007), p. 134.
[19]Y. Zhao, G. C. Wang, and T.-M. Lu, *Experimental Methods in the Physical Sciences: Characterization of Amorphous and Crystalline Rough Surface: Principles and Applications* (Academic, San Diego, 2001), Vol. 37.
[20]Y. H. Xie, G. H. Gilmer, C. Roland, P. J. Silverman, S. K. Buratto, J. Y. Cheng, E. A. Fitzgerald, A. R. Kortan, S. Schuppler, M. A. Marcus, and P. H. Citrin, Phys. Rev. Lett. **73**, 3006 (1994).
[21]J. Tersoff and F. K. LeGoues, Phys. Rev. Lett. **72**, 3570 (1994).
[22]L. Thevenod, M. Cassé, M. Mouis, G. Reimbold, F. Fillot, B. Guillaumot, and F. Boulanger, Microelectron. Eng. **80**, 11 (2005).
[23]S. M. Goodnick, D. K. Ferry, C. W. Wilmsen, Z. Liliental, D. Fathy, and O. L. Krivanek, Phys. Rev. B **32**, 8171 (1985).
[24]T. Ando, A. B. Fowler, and F. Stern, Rev. Mod. Phys. **54**, 437 (1982).
[25]M. V. Fischetti and S. E. Laux, Phys. Rev. B **48**, 2244 (1993).
[26]M. V. Fischetti, J. Appl. Phys. **89**, 1232 (2001).
[27]M. V. Fischetti, Z. Ren, P. M. Solomon, M. Yang, and K. Rim, J. Appl. Phys. **94**, 1079 (2003).
[28]*ATLAS Users manual, version 5.11.34.C* (Silvaco, Santa Clara, CA, 2006).
[29]Since experimental as well as theoretical results (see, e.g., Ref. 41) show that [100]-(001) and [110]-(001) long-channel electron effective mobility are almost the same, for simplicity we take the axis [100], [010], and [001] to set the coordinate system. Indeed, with this choice all valleys have a diagonal effective mass tensor (Ref. 42).
[30]D. Esseni, A. Abramo, L. Selmi, and E. Sangiorgi, IEEE Trans. Electron Devices **50**, 2445 (2003).
[31]B. K. Ridley, J. Phys. C **15**, 5899 (1982).
[32]C. Jacoboni and L. Reggiani, Rev. Mod. Phys. **55**, 645 (1983).
[33]F. Gámiz, J. B. Roldán, J. A. López-Villanueva, P. Cartujo-Cassinello, and J. E. Carceller, J. Appl. Phys. **86**, 6854 (1999).
[34]F. Gámiz and J. B. Roldán, J. Appl. Phys. **94**, 392 (2003).
[35]S. Saito, K. Torii, Y. Shimamoto, S. Tsujikawa, H. Hamamura, O. Tonomura, T. Mine, D. Hisamoto, T. Onai, J. Yugami, M. Hiratani, and S. Kimura, Appl. Phys. Lett. **84**, 1395 (2004).
[36]D. Esseni, IEEE Trans. Electron Devices **51**, 394 (2004).
[37]P. F. Maldague, Surf. Sci. **73**, 296 (1978).
[38]M. V. Fischetti and S. E. Laux, J. Appl. Phys. **80**, 2234 (1996).
[39]M. M. Rieger and P. Vogl, Phys. Rev. B **48**, 14276 (1993).
[40]D. Esseni, M. Mastrapasqua, G. Celler, C. Fiegna, L. Selmi, and E. Sangiorgi, IEEE Trans. Electron Devices **48**, 2842 (2001).
[41]M. V. Fischetti, S. Narayanan, T O'Reagan, and C. Sachs, ECS Trans. **3**, 33 (2006).
[42]A. Rahman, M. S. Lundstrom, and A. W. Ghosh, J. Appl. Phys. **97**, 053702 (2005).
[43]R. Brunetti, C. Jacoboni, F. Nava, L. Reggiani, G. Bosman, and R. J. J. Zijlstra, J. Appl. Phys. **52**, 6713 (1981).